

Aligning Oxygen Vacancies Oriently: Electric-Field Inducing Conductive Channels in TiO₂ Film to boost Photocatalytic Conversion of CO₂ into CO

Junming Li

Nanjing University

Wenxia Su

Nanjing University

Jun Li

Nanjing University

Lu Wang

Nanjing University

Jun Ren

Nanjing University

Sheng Zhang

Nanjing University

Pengtao Cheng

Nanjing University

Hong Hong

Nanjing University

Dunhui wang (✉ wangdh@hdu.edu.cn)

Nanjing University

Yong Zhou

Nanjing University

Wenbo Mi

Tianjin University <https://orcid.org/0000-0002-9108-9930>

Youwei Du

Nanjing University

Article

Keywords: Oxide Semiconductors, Photocatalysis, Electron-hole Pairs, Carrier Migration Rate, CO Yield

Posted Date: November 16th, 2020

DOI: <https://doi.org/10.21203/rs.3.rs-104327/v1>

License:  This work is licensed under a Creative Commons Attribution 4.0 International License.

[Read Full License](#)

Abstract

Oxide semiconductors are widely used in the photocatalytic fields and introducing oxygen vacancies is an effective strategy to reduce the band gap, and consequently, improve their photocatalytic efficiency. However, oxygen vacancies in bulk often act as the recombination centers of electron-hole pairs, which would accelerate the recombination of electron-hole pairs and reduce carrier migration rate. Therefore, for achieving excellent photocatalytic performance in oxide photocatalysts, taking good advantage of oxide vacancies is very crucial. In this paper, we propose a strategy of electric field treatment and apply it in the TiO₂ film with oxygen vacancies to promote the photocatalytic efficiency. After treated by an electric field, conductive channels consisting of oxygen vacancies are formed in TiO₂ film, which makes the resistance greatly decreased by almost 6×10^3 times. In the photocatalytic CO₂ reduction reaction, the yield of CO in the electric-field-treated TiO₂ film can reach up to $1.729 \text{ mmol} \cdot \text{g}^{-1} \cdot \text{h}^{-1}$, which is one of the best performance among the reported TiO₂-based catalysts. This work provides an effective and feasible way for enhancing photocatalytic activity through electric field and this method is promising to be widely used in the field of catalysis.

Introduction

With the destruction of the environment and the depletion of fossil fuels, the application of photocatalysis to produce clean energy and useful chemicals has attracted more and more attention¹⁻⁴. However, the photocatalytic performance is far from satisfying the practical application requirements due to the narrow light response, fast carrier recombination and low charge mobility. Thus, enormous efforts have been made to solve aforementioned problems and explore the photocatalysts with high performance. For example, by doping defects, the band gap of the semiconducting photocatalysts can be reduced, and as a result, the optical response range is broadened, which leads to many more photogenerated carriers to participate in the photocatalytic processes^{5,6}; As for the suppression of charge recombination, metal or non-metal loading and construction of heterojunction are designed to create the built-in electric fields, in which the electrons and holes are separated and transfer to spatially separated locations⁷⁻¹⁰; In the case of improving the carrier mobility, it is reported that under the action of external fields, the carrier migration can be speeded up, and consequently, more carriers would participate in the catalytic reaction per unit time¹¹.

Oxide semiconductors are the most common photocatalysts and introducing oxygen vacancy (OV) is a usually used method to improve their photocatalytic performance, which can be ascribed to the reduced band gap¹²⁻¹⁶. For instance, Mao et al. reported that the black TiO₂ with large amount of OVs could absorb visible and infrared light and broaden the light response range¹⁷. Huang et al. introduced that OVs would narrow the band gap and improve visible light photocatalytic performance of ZnO¹⁸. However, in various cases, the bulk OVs would serve as the recombination centers of carriers, which accelerate the recombination of electron-hole pairs and reduce carrier migration rate¹⁹⁻²¹. It seems that although the light response range in the oxide photocatalysts can be remarkably broadened by introducing the OVs,

their photocatalytic performance needs to be further improved. Therefore, making good use of OV's to promote charge separation and improve carrier mobility simultaneously is a giant challenge for achieving excellent photocatalytic activities in the oxide photocatalysts.

It is reported that under the action of an external electric field, OV's in some oxide semiconductors can be oriented along the electric field direction to form conductive channels, and consequently, greatly reduce the system resistivity²²⁻²⁴. This phenomenon is called as resistance switching (RS) effect^{25,26}. The composition of the RS device is a metal/oxide/metal sandwich structure, where the metals act as the electrodes. The mechanism of RS is schematically illustrated in Fig. 1. As shown in Fig. 1a, the original state of the sample is considered a high resistance state (HRS), in which some OV's are scattered in the oxide. Under the action of an electric field, oxygen ions move to anode electrode and leave the OV's staying at their original location. As the electric field rises, the number of OV's continues to increase, and the conductive filaments (i.e. conductive channels) consisting of OV's are gradually formed along the direction of electric field. Until the OV's align in the film from bottom to the top, the device turns into a low resistance state (LRS), which is shown in Fig. 1b. As a result, conductive channels consisting of OV's are constructed in the LRS film, which can accelerate the carrier migration, and consequently, facilitate the photocatalytic reaction.

TiO₂ has attracted extensive research interests in the field of photocatalysis owing to several outstanding advantages such as high photocatalytic activity, good photostability, non-toxicity, earth abundance and low cost²⁷⁻²⁹. It can show broadened light response range by introducing a lot of OV's^{12,13}, but faces the same problems mentioned above. As we know, TiO₂ is a well-studied RS material based on the mechanism of conductive filaments^{30,31}, which provides a good opportunity for us to study the effect of OV's conductive channels on the photocatalytic performance. In this paper, the TiO₂ film with some OV's is prepared in a low oxygen pressure environment. After treated by an electric field, the conductive filaments consisting of OV's are formed due to the RS effect, which makes the resistance of TiO₂ film decreased by almost 6 × 10³ times. Thus the OV's conductive filaments would provide many highways in bulk to speed up the migration of the photogenerated carriers, which is very meaningful for improving photocatalytic activity. As expected, the electric-field-treated TiO₂ film show excellent photocatalytic performance of CO₂ reduction, and the CO production rate reaches up to 1.729 mmol·g_{cat}⁻¹·h⁻¹.

Results And Discussion

Composition and structure of device

TiO₂ film is deposited onto a Pt/SiO₂/Si substrate using pulsed laser deposition (PLD). Subsequently, Au circular electrodes are deposited using an ion sputtering instrument onto TiO₂ film with a shadow mask. The formation process of Au/TiO₂/Pt/SiO₂/Si device is shown in Fig. 2a, in which Au and Pt act as the top and bottom electrodes, respectively. It is worth mentioning that Au electrode not only serves as the electrode, but also plays a role of co-catalyst for promoting the reduction of CO₂ to CO³². Fig. 2b shows

the surface image of Au/TiO₂/Pt device. It is observed that Au circular electrodes with a diameter of about 100 μm are on the surface of the TiO₂ film. The cross section SEM image of the device with Au electrode is shown in Fig. 2c. It is observed that the thicknesses of TiO₂ film and Au electrode are approximately 200 and 40 nm, respectively. The XRD pattern of the device is shown in Supplementary Fig. 1a. In addition to the diffraction peaks of the substrate, a group of diffraction peaks with (103), (004), (112) and (200) peaks of anatase (JCPDS No. 21-1272), (101) peak of rutile (JPCDS No. 21-1276), as well as (111) diffraction peak of Pt are observed, indicating that the TiO₂ film has mixed phases of anatase and rutile. The phase ratio of the TiO₂ film is analyzed by Jade and the analysis result is shown in Supplementary Fig. 1b, in which the weight percentage (wt %) of anatase to rutile is 94% : 6%.

Characteristic of RS effect

The evolution process of RS effect in TiO₂ film is illustrated in Fig. 3a. The original state of TiO₂ film is HRS. When the positive sweeping voltage is applied to the device, the current gradually increases and shows a sudden jump at 2.5 V, indicating the switching from HRS to LRS (Set process). This phenomenon corresponds to the formation of OV's conductive filaments, which is shown in Fig. 1b. During this process, a compliance current of 10 mA is adopted to avoid permanent dielectric breakdown of the device. As the voltage polarity is changed and the negative sweeping voltage is applied, the device returns to HRS with the current dropping sharply at -1.5 V (Reset process). At this situation, the oxygen ions will move to the opposite direction and combine with the OV, leading to the rupture of the conductive filaments. As a result, the device switches to HRS, which is shown in Fig. 1a. The resistance state of the Au/TiO₂/Pt device can switch between LRS and HRS by changing the voltage polarity, displaying a bipolar RS behavior, which is consistent with the earlier reports of TiO₂-based RS devices^{33,34}. It is worth noting that the RS effect of the device is nonvolatile, i.e., TiO₂ can maintain LRS or HRS after the applied electric field is switched off, which is very meaningful for the practical applications^{35,36}. In order to study the durability of RS behavior, an endurance test on LRS and HRS of the device is performed. As shown in Fig. 3b, both LRS and HRS samples can remain stable without any obvious degradation even after 10⁴ s, demonstrating that the device has good retention performance. More importantly, the on/off ratio ($R_{\text{HRS}}/R_{\text{LRS}}$) is larger than 6×10^3 , which implies that TiO₂ in LRS possesses high conductivity and is promising to show excellent photocatalytic performance.

Structure and oxygen vacancy characterization of LRS and HRS samples

The valence state of elements in TiO₂ film and the presence of OVs are analyzed by X-ray photoelectron spectroscopy (XPS). Fig. 4a shows the XPS spectrum of Ti 2*p* level for both LRS and HRS samples. The peaks locating at 458.8 and 464.6 eV correspond to the Ti 2*p*_{3/2} and Ti 2*p*_{1/2} bands, respectively, which are typical energy level peaks with Ti⁴⁺ characteristics^{37,38}. Additionally, the TiO₂ film possesses shoulder peaks near 457.6 eV and 463.6 eV at the lower energy sides, which are assigned to Ti³⁺ species³⁹. As we know, the generation of Ti³⁺ is usually associated with the formation of OVs⁴⁰. As shown in Fig. 4b, the

shoulder peak at 531.7 eV can be deemed as the defect site with low oxygen coordination (i.e. OV)⁴¹. Considering the difference of peak areas at 531.7 eV, the OV concentration of LRS sample is larger than that of HRS sample⁴¹, suggesting that the application of electric field can generate extra OVs in LRS sample. Based on XPS data, the atom ratio of Ti³⁺/Ti⁴⁺ and the concentration percentage of OV are estimated by the quantitative analyses of Ti³⁺/Ti⁴⁺ peaks and O/Ti atomic percentage, which are shown in Supplementary Table 1.

The structural properties of TiO₂ film are investigated by Raman spectroscopy. As shown in Fig. 4c, the peaks around 143, 195, 635, 399, and 515 cm⁻¹ belong to E_g, E_g, E_g, B_{1g}, and A_{1g} modes of anatase, respectively. Moreover, the band at 320 cm⁻¹ is observed, which can be assigned to a two-phonon scattering band of anatase⁴². In addition to the peaks of anatase, the weak peaks at 245 and 430 cm⁻¹ are ascribed to the two-phonon scattering and E_g modes of rutile, respectively⁴³. Thus we can deduce that the main phase of TiO₂ film is anatase, which is consistent with the result of XRD. It is reported that the existence of OVs can be confirmed by Raman shift either¹³. As shown in Fig. 4d, the E_g peaks of HRS and LRS samples locate at 142.5 and 144.1 cm⁻¹, respectively. Therefore, an evident shift of E_g peak is presented in LRS sample, which can be attributed to the increased amount of OVs in LRS sample^{44,45}. Meanwhile, the E_g peak of LRS sample is wider than that of HRS sample, implying that the degree of lattice disorder is increased by more bulk OVs^{46,47}.

In order to detect the distribution of the OVs, a two-dimensional Raman spectrogram around 143 cm⁻¹ is investigated in the samples. As shown in Fig. 5, the two-dimensional Raman spectra exhibit different brightness. Here, the change of brightness represents the shift of Raman peak. According to the result of Fig. 4d, the Raman peak of LRS sample with more OVs has higher wavenumber. As a result, the darker regions represent the lower OV concentrations of HRS sample (Fig. 5a) and the brighter regions stand for the higher OV concentrations of LRS sample (Fig. 5b). Combined with the analysis of the RS mechanism, the OVs conductive filaments would locate at the brighter regions in Fig. 5b.

The optical properties of HRS and LRS samples are investigated by UV-visible diffuse reflectance absorption spectroscopy in Supplementary Fig. 2a. Compared with the optical absorption spectra of TiO₂ film without OVs⁴⁸, the spectra of LRS and HRS samples exhibit long wavelength absorption, which extends to visible light and infrared light. In order to exclude the influence of Au on the absorption peaks, the UV-visible absorption spectrum of TiO₂ film without Au electrode is characterized in Supplementary Fig. 2b. It is obvious that the absorption spectrum of pure TiO₂ film is similar to that of HRS and LRS samples. This result implies that the effect of Au electrodes on the long wavelength absorption can be almost neglected. As a result, the long wavelength absorption of LRS and HRS samples are mainly attributed to the presence of OVs in the TiO₂ films. Furthermore, the LRS sample demonstrates wider range of light absorption than that of HRS sample due to the more OVs^{49,50}.

Photocatalytic performance of CO₂ reduction

The photocatalytic performances of the samples are evaluated via CO₂ photoreduction under simulated sunlight irradiation. Prior to irradiation, ultra-pure CO₂ gas is flowed into the reaction chamber and the samples are kept in the reaction atmosphere for several hours to ensure that the adsorption of gas molecules is completed. During the photoreduction process, CO is detected as the main product. Fig. 6a shows the time dependence of the production of CO for LRS and HRS samples. It is obvious that with the increase of time, the CO evolution of HRS sample increases almost linearly. As shown in Fig. 6b, the CO production rate of HRS sample is probably 1.007 mmol·g_{cat}⁻¹·h⁻¹. As for LRS sample, it exhibits similar catalytic behavior to HRS sample, but its photocatalytic performance is significantly improved. After the irradiation for 4 h, the CO production rate of LRS sample is as high as 1.729 mmol·g_{cat}⁻¹·h⁻¹, which is 172% higher than that of HRS sample. Therefore, the electric field treatment is a very effective method for achieving excellent photocatalytic performance. As far as we know, the CO yield of LRS sample is one of the best among the reported TiO₂-based catalysts and the detailed results are listed in Table 1. Furthermore, LRS and HRS samples can demonstrate excellent stability toward CO₂ photoreduction. As shown in Fig. 6c, no significant deterioration is detected for the photocatalytic activity after four cycles of repeated tests.

Photoelectrochemical properties of LRS and HRS samples

The photoluminescence (PL) spectroscopy is used to evaluate the carrier separation/recombination performance⁵¹. As shown in Fig. 7a, the samples of HRS and LRS display strong emission peaks in the wavelength range of 550-825 nm. It is obvious that the peak intensity of LRS sample is relatively low, indicating that the carrier recombination of LRS sample is slower than that of HRS sample. The time-resolved photoluminescence spectroscopy is measured to reveal the lifetime of carriers. As shown in Fig. 7b, the average lifetime of carriers in HRS sample is 1.50 ns. However, after the treatment of electric field, the average lifetime in LRS sample increase to 1.69 ns, which is beneficial to enhance photocatalytic performance. The linear voltammetry scan curve of HRS and LRS samples at the cathode is shown in Supplementary Fig. 3. It is observed that the photocurrent of LRS sample is stronger than that of HRS sample, indicating that the electrons of LRS sample have a faster transfer speed and a shorter migration time to the surface owing to the lower resistivity. Fig. 7c shows the transient chronoamperometry of the samples, in which all the samples display constant on-off responses. Obviously, the photocurrent density of LRS sample is 2.0 times higher than that of HRS sample, suggesting that LRS sample has higher electron-hole separation efficiency. The Nyquist plots of the electrochemical impedance spectroscopy are carried out at the open circuit potential, which is shown in Fig. 7d. Compared with the HRS sample, LRS sample shows the smaller semicircles in the Nyquist plot, suggesting the lower charge transfer resistance and the higher charge mobility⁵².

To gain further insight into the charge-transfer process and the impact of electric field on the electronic properties of TiO₂, the electrochemical impedance measurements of LRS and HRS samples are performed at 1 kHz. Supplementary Fig. 4 shows the Mott-Schottky plots of samples, in which the positive slopes can be observed as expected for n-type semiconductors³⁷. Different from HRS sample, a

substantially shallow slope for LRS sample with higher OV concentration can be obtained, suggesting the increase of carrier density. Here carrier density can be calculated from the slope of the Mott-Schottky plots using the equation (1)^{53,54}.

$$N_d = (2/e_0\epsilon\epsilon_0)[d/(1/C^2)/dV]^{-1} \quad (1)$$

where e_0 is the electronic charge, ϵ is the dielectric constant of TiO_2 ($\epsilon_{\text{anatase}} = 55$, $\epsilon_{\text{rutile}} = 170$)^{55,56}, ϵ_0 is the dielectric constant of vacuum, N_d is the carrier density, and V is the external bias voltage on the electrode. The calculated carrier density of HRS and LRS samples are $5.7 \times 10^{18} \text{ cm}^{-3}$ and $4.0 \times 10^{19} \text{ cm}^{-3}$, respectively. Here the carrier density of LRS sample is 7 times higher than that of HRS sample, which is beneficial to improve the electron-hole pair separation and transport efficiency⁵⁴. Based on above analysis, LRS sample possesses quite excellent charge separation and transfer efficiency, which can significantly improve the activity of CO_2 reduction.

Photocatalytic mechanism of CO_2 reduction in LRS system

To understand the influence of OVs on the band gap of the non-conductive filament region (NCFR) and the conductive filament region (CFR), the electronic density of states and band structure of anatase (because 94% of the content in TiO_2 film has this structure) with OVs are calculated by first-principles calculations based on density functional theory. Based on the data of OV concentration from the XPS results, the structure models, density of states and band structure of TiO_2 with different OV concentrations are shown in Fig. 8a, Fig. 8b and Supplementary Fig. 5, respectively. In the present model, one OV per 16 O atoms is set in a $2 \times 1 \times 1$ supercell, which corresponds to the NCFR with fewer OVs. As for the CFR with more OVs, two OVs per 16 O atoms are set. The valence band edge of TiO_2 is dominated by O $2p$ states, while the conduction band edge is formed from Ti $3d$ states. According to the calculation results, the values of band gap for NCFR and CFR are 1.62 eV and 1.5 eV, respectively, suggesting that the light absorption range of CFR is larger. Furthermore, the potentials of conduction band (CB) minimum and valence band (VB) maximum in CFR are lower than those in NCFR. Therefore, a homojunction can be formed between NCFR and CFR in LRS sample, which is shown in Fig. 8c. In this homojunction, the electrons in the CB of NCFR would migrate to the CB of CFR and the holes in the VB of CFR transfer to the VB of NCFR, which leads to the efficient spatial charge separation. Different from the earlier reports^{7,57}, the junctions in LRS sample are constructed not only at the surface but also in bulk, which is conducive to the bulk charge separation.

Based on the experimental and theoretical results mentioned above, we can investigate the origin of excellent photocatalytic performance in LRS sample. Fig. 9 shows the schematic illustration of photocatalytic process of CO_2 reduction. Due to the contribution of large amount of OVs in LRS TiO_2 sample, the band gap is reduced, which broadens the light absorption range. As a result, many photogenerated carriers can participate in the photocatalytic reaction, which is one of the reasons for excellent photocatalytic performance. Secondly, after the treatment of electric field, the OVs align along

the electric field direction and form some conductive filaments. As mentioned above, the conductive filament consisting of OV's reduces the band gap and a homojunction can be constructed between CFR and NCFR in LRS sample, which is conducive to promote the separation of electrons and holes. Finally and most importantly, the photogenerated carriers can migrate rapidly to the surface along the conductive filaments to participate in the reduction reaction. Under the synergistic effect of above three favorable conditions, an excellent photocatalytic performance of CO₂ reduction is realized in LRS sample.

Summary

TiO₂ film with OV's is prepared by PLD to investigate the photocatalytic reduction of CO₂. After the treatment of electric field, TiO₂ film can switch from HRS to LRS due to the formation of conductive filaments consisting of OV's. The existence of conductive filaments brings about three advantages for improving photocatalytic properties of LRS sample. First, the light absorption range is broadened which leads to many more photogenerated carriers to participate in photocatalytic reaction. Second, homojunctions are constructed between CFRs and NCFRs, which promotes space charge separation. And the last is a distinctive advantage, conductive channels based on OV's are built, which accelerates the migration of carriers to the film surface. This work provides a novel approach for enhancing photocatalytic activity with the treatment of electric field. Moreover, this method of electric-field-induced high conductivity in semiconductive/insulative catalysts is promising to be widely used in the catalytic fields.

Methods

Preparation of Au/TiO₂/Pt device. TiO₂ film was deposited on Pt/SiO₂/Si substrate using PLD with a 248 nm KrF excimer laser at 3Hz. The target material has a stoichiometric ratio and the base vacuum of the chamber was below 1.0 × 10⁻⁵ Pa. During the deposition of the film, the substrate temperature was maintained at 600 °C, whereas the oxygen pressure was 20 Pa. After deposition, the film was annealed *in situ* at 600 °C for 30 min. Circular Au top electrodes with diameter of 100 μm were deposited on TiO₂ film with a shadow mask using an ion sputtering instrument.

Material characteristics. The crystal structure of the sample was characterized by X-ray diffraction spectrometer (Cu Kα, td-3500, Tongda). The thickness of the film was measured by a field emission scanning electron microscopy (GeminiSEM 500, ZEISS, Germany). X-ray photoelectron spectroscopy measurement was performed on a Phi5000 VersaProbe (ULVAC-PHI, Japan) using 200 W monochromated Al Kα radiation as the X-ray source. The standard C1s peak was used as a reference for correcting the shift. Raman and PL spectra/mapping were carried out by confocal Raman and photoluminescence techniques with a 532 nm laser as the light source (*Alpha 300R, WITec*, Germany). The PL lifetime measurements were performed using a PL spectrometer (FLS 920, Edinburgh, UK) at an excitation wavelength of 375 nm. The UV-visible diffuse reflectance spectra (UV-vis DRS) of

samples were recorded on an UV-vis-NIR spectrophotometer (TU-1900, Puxi). The electrical properties of the samples were measured with Keithley2410 and a dual probe configuration was performed.

Photocatalytic CO₂ reduction reaction. Photocatalytic reactions were performed in a reactor with a quartz window on the top. The device with an area of 0.5 cm² was placed on a Teflon catalyst holder without being immersed in water. The volume of reaction system was about 440 ml. Before the irradiation, ultra-pure CO₂ gas was continuously flowed into the CO₂-reduction chamber for half an hour to ensure that no impurity gas exists in the reaction system. Subsequently, 0.4 mL of deionized water was injected into the bottom of the reactor. The samples were kept in the reaction atmosphere without irradiation for several hours to ensure that the adsorption of gas molecules was complete. During the photoreaction, the chamber was irradiated with a 300 W Xenon (Xe) lamp. The photocatalytic reaction was carried out for 4 h. The gaseous products in chamber were collected each hour by a sampling syringe (1 mL) and then syringed into the gas chromatography (GC-2014, Shimadzu Corp., Japan) for analysis.

Photoelectrochemical measurements. Photoelectrochemical measurements were carried out with an electrochemical workstation (CHI760D) using a standard three-electrode electrochemical cell. The working electrode is Au/TiO₂/Pt device, with a platinum foil as the counter electrode and an Ag/AgCl electrode as the reference. A sodium sulfate solution (0.1 M) was employed as the electrolyte, and a 300 W Xe lamp as the light source. Electrochemical impedance spectroscopy (EIS) and Mott-Schottky plots were carried out at the open circuit potential.

DFT calculations. All first-principles calculations based on density functional theory (DFT) were implemented using the Vienna *Ab-initio* Simulation Package (VASP, version 5.3) within the general gradient approximation (GGA) parametrized with the Perdew-Burke-Ernzerhof (PBE) method⁵⁸⁻⁶⁰. The structures were relaxed until forces were converged within 0.01 eV Å⁻¹, and the convergence criterion for total energy was 10⁻⁴ eV. The Brillouin zone was sampled with a 5×5×2 *k*-point grid mesh for the unit cell⁶¹. The plane wave with a kinetic energy cutoff was 600 eV for the structure optimization.

Data availability

The data that support the findings of this study are available from the corresponding author upon request.

References

- 1 Rao, H., Schmidt, L. C., Bonin, J. & Robert, M. Visible-light-driven methane formation from CO₂ with a molecular iron catalyst. *Nature* **548**, 74-77 (2017).
- 2 Voiry, D., Shin, H. S., Loh, K. P. & Chhowalla, M. Low-dimensional catalysts for hydrogen evolution and CO₂ reduction. *Nat. Rev. Chem.* **2**, 17105 (2018).

- 3 Habisreutinger, S. N., Schmidt-Mende, L. & Stolarczyk, J. K. Photocatalytic reduction of CO₂ on TiO₂ and other semiconductors. *Angew. Chem. Int. Ed.* **52**, 7372-7408 (2013).
- 4 Woolerton, T. W. *et al.* Efficient and clean photoreduction of CO₂ to CO by enzyme-modified TiO₂ nanoparticles using visible light. *J. Am. Chem. Soc.* **132**, 2132-2133 (2010).
- 5 Wang, Y. *et al.* Increasing solar absorption of atomically thin 2D carbon nitride sheets for enhanced visible-light photocatalysis. *Adv. Mater.* **31**, 1807540 (2019).
- 6 Pan, X., Yang, M. Q., Fu, X., Zhang, N. & Xu, Y. J. Defective TiO₂ with oxygen vacancies: synthesis, properties and photocatalytic applications. *Nanoscale* **5**, 3601-3614 (2013).
- 7 Li, J. Y., Dong, X. A., Sun, Y. J., Cen, W. L. & Dong, F. Facet-dependent interfacial charge separation and transfer in plasmonic photocatalysts. *Appl. Catal. B Environ.* **226**, 269-277 (2018).
- 8 Xiang, Q. J., Cheng, B. & Yu, J. G. Graphene-based photocatalysts for solar-fuel generation. *Angew. Chem. Int. Ed.* **54**, 11350-11366 (2015).
- 9 Wang, H. L. *et al.* Semiconductor heterojunction photocatalysts: design, construction, and photocatalytic performances. *Chem. Soc. Rev.* **43**, 5234-5244 (2014).
- 10 Moniz, S. J. A., Shevlin, S. A., Martin, D. J., Guo, Z. X. & Tang, J. W. Visible-light driven heterojunction photocatalysts for water splitting - a critical review. *Energy Environ. Sci.* **8**, 731-759 (2015).
- 11 Li, J. *et al.* Enhanced photocatalytic performance through magnetic field boosting carrier transport. *ACS Nano* **12**, 3351-3359 (2018).
- 12 Gordon, T. R. *et al.* Nonaqueous synthesis of TiO₂ nanocrystals using TiF₄ to engineer morphology, oxygen vacancy concentration, and photocatalytic activity. *J. Am. Chem. Soc.* **134**, 6751-6761 (2012).
- 13 Naldoni, A. *et al.* Effect of nature and location of defects on bandgap narrowing in black TiO₂ nanoparticles. *J. Am. Chem. Soc.* **134**, 7600-7603 (2012).
- 14 Lv, Y. H., Liu, Y. F., Zhu, Y. Y. & Zhu, Y. F. Surface oxygen vacancy induced photocatalytic performance enhancement of a BiPO₄ nanorod. *J. Mater. Chem. A* **2**, 1174-1182 (2014).
- 15 Li, C. Q. *et al.* Oxygen vacancy engineered SrTiO₃ nanofibers for enhanced photocatalytic H₂ production. *J. Mater. Chem. A* **7**, 17974-17980 (2019).
- 16 Wang, Y. T. *et al.* Rational construction of oxygen vacancies onto tungsten trioxide to improve visible light photocatalytic water oxidation reaction. *Appl. Catal. B: Environ.* **239**, 398-407 (2018).
- 17 Chen, X. B., Liu, L., Yu, P. Y. & Mao, S. S. Increasing solar absorption for photocatalysis with black hydrogenated titanium dioxide nanocrystals. *Science* **331**, 746-750 (2011).

- 18 Wang, J. P. *et al.* Oxygen vacancy induced band-gap narrowing and enhanced visible light photocatalytic activity of ZnO. *ACS Appl. Mater. Interfaces* **4**, 4024-4030 (2012).
- 19 Choi, W., Termin, A. & Hoffmann, M. R. The role of metal ion dopants in quantum-sized TiO₂: correlation between photoreactivity and charge carrier recombination dynamics. *J. Phys. Chem.* **98**, 13669-13679 (1994).
- 20 Iván M. S. *et al.* Photoelectrochemical behavior of nanostructured TiO₂ thin-film electrodes in contact with aqueous electrolytes containing dissolved pollutants: a model for distinguishing between direct and indirect interfacial hole transfer from photocurrent measurements. *J. Phys. Chem. B* **109**, 3371-3380 (2005).
- 21 Fujishima, A., Rao, T. N. & Tryk, D. A. Titanium dioxide photocatalysis. *J. Photochem. Photobiol. C* **1**, 1-21 (2000).
- 22 Yan, Z., Guo, Y. Y., Zhang, G. Q. & Liu, J. M. High-performance programmable memory devices based on Co-doped BaTiO₃. *Adv. Mater.* **23**, 1351-1355 (2011).
- 23 Younis, A., Chu, D., Mihail, I. & Li, S. Interface-engineered resistive switching: CeO₂ nanocubes as high performance memory cells. *ACS Appl. Mater. Interfaces* **5**, 9429-9434 (2013).
- 24 Choi, B. J. *et al.* Study on the resistive switching time of TiO₂ thin films. *Appl. Phys. Lett.* **89**, 012906 (2006).
- 25 Yang, J. J. *et al.* The mechanism of electroforming of metal oxide memristive switches. *Nanotechnology* **20**, 215201 (2009).
- 26 Wen, J. H. *et al.* Nonvolatile control of magnetocaloric operating temperature by low voltage. *ACS Appl. Mater. Interfaces* **10**, 15298-15303 (2018).
- 27 Chen, X. B. & Mao, S. S. Titanium dioxide nanomaterials: synthesis, properties, modifications, and applications. *Chem. Rev.* **107**, 2891-2959 (2007).
- 28 G. Liu *et al.* Enhanced photoactivity of oxygen-deficient anatase TiO₂ sheets with dominant {001} facets. *J. Phys. Chem. C* **113**, 21784-21788 (2009).
- 29 Thompson, T. L. & Yates, J. T. TiO₂-based photocatalysis: surface defects, oxygen and charge transfer. *Top. Catal.* **35**, 197-210 (2005).
- 30 Choi, B. J. *et al.* Resistive switching mechanism of TiO₂ thin films grown by atomic-layer deposition. *J. Appl. Phys.* **98**, 033715 (2005).

- 31 Yin, X. B., Tian, K., Tan, Z. H., Yang, R. & Guo, X. Polarity reversal in the bipolar switching of anodic TiO₂ film. *J. Electrochem. Soc.* **162**, E271-E275 (2015).
- 32 Peterson, A. A. & Nørskov, J. K. Activity descriptors for CO₂ electroreduction to methane on transition-metal catalysts. *J. Phys. Chem. Lett.* **3**, 251-258 (2012).
- 33 Zhu, Y. D. *et al.* Nonvolatile bipolar resistive switching in an Ag/TiO₂/Nb : SrTiO₃/In device. *J. Phys. D: Appl. Phys.* **45**, 375303 (2012).
- 34 Fujimoto, M. *et al.* TiO₂ anatase nanolayer on TiN thin film exhibiting high-speed bipolar resistive switching. *Appl. Phys. Lett.* **89**, 223509 (2006).
- 35 Yu, Z. Q., Qu, X. P., Yang, W. P., Peng, J. & Xu, Z. M. Hydrothermal synthesis and memristive switching behaviors of single-crystalline anatase TiO₂ nanowire arrays. *J. Alloys Compd.* **688**, 294-300 (2016).
- 36 Tsunoda, K. *et al.* Bipolar resistive switching in polycrystalline TiO₂ films. *Appl. Phys. Lett.* **90**, 113501 (2007).
- 37 Wang, G. M. *et al.* Hydrogen-treated TiO₂ nanowire arrays for photoelectrochemical water splitting. *Nano Lett.* **11**, 3026-3033 (2011).
- 38 Cao, N. *et al.* Doping strain induced bi-Ti³⁺ pairs for efficient N₂ activation and electrocatalytic fixation. *Nat. Commun.* **10**, 2877 (2019).
- 39 Wu, S. M. *et al.* Homojunction of oxygen and titanium vacancies and its interfacial n-p effect. *Adv. Mater.* **30**, 1802173 (2018).
- 40 Xia, T., Zhang, W., Murowchick, J. B., Liu, G. & Chen, X. B. A facile method to improve the photocatalytic and lithium-ion rechargeable battery performance of TiO₂ nanocrystals. *Adv. Energy Mater.* **3**, 1516-1523 (2013).
- 41 Zhu, J. H. *et al.* Bilayer nanosheets of unusual stoichiometric bismuth oxychloride for potassium ion storage and CO₂ reduction. *Nano Energy* **75**, 104939 (2020).
- 42 Ohsaka, T., Izumi, F. & Fujiki, Y. Raman spectrum of anatase, TiO₂. *J. Raman Spectrosc.* **7**, 321-324 (1978).
- 43 Zhang, J., Li, M. J., Feng, Z. C., Chen, J. & Li, C. UV Raman spectroscopic study on TiO₂. I. Phase transformation at the surface and in the bulk. *J. Phys. Chem. B* **110**, 927-935 (2006).
- 44 Li, G. S. *et al.* Ionothermal synthesis of black Ti³⁺-doped single-crystal TiO₂ as an active photocatalyst for pollutant degradation and H₂ generation. *J. Mater. Chem. A* **3**, 3748-3756 (2015).

- 45 Zhang, H. *et al.* Insights into the effects of surface/bulk defects on photocatalytic hydrogen evolution over TiO₂ with exposed {001} facets. *Appl. Catal. B Environ.* **220**, 126-136 (2018).
- 46 Zhou, W. *et al.* Ordered mesoporous black TiO₂ as highly efficient hydrogen evolution photocatalyst. *J. Am. Chem. Soc.* **136**, 9280-9283 (2014).
- 47 Ou, G. *et al.* Tuning defects in oxides at room temperature by lithium reduction. *Nat. Commun.* **9**, 1302 (2018).
- 48 Asahi, R., Morikawa, T., Ohwaki, T., Aoki, K. & Taga, Y. Visible-light photocatalysis in nitrogen-doped titanium oxides. *Science* **293**, 269-271 (2001).
- 49 Li, K. *et al.* In-situ-reduced synthesis of Ti³⁺ self-doped TiO₂/g-C₃N₄ heterojunctions with high photocatalytic performance under LED light irradiation. *ACS Appl. Mater. Interfaces* **7**, 9023-9030 (2015).
- 50 Dong, J. Y. *et al.* Defective black TiO₂ synthesized via anodization for visible-light photocatalysis. *ACS Appl. Mater. Interfaces* **6**, 1385-1388 (2014).
- 51 Cai, J. M. *et al.* Synergistic effect of titanate-anatase heterostructure and hydrogenation-induced surface disorder on photocatalytic water splitting. *ACS Catal.* **5**, 1708-1716 (2015).
- 52 Zhang, K. F. *et al.* Black N/H-TiO₂ nanoplates with a flower-like hierarchical architecture for photocatalytic hydrogen evolution. *ChemSusChem* **9**, 2841-2848 (2016).
- 53 Hu, W. Y. *et al.* Facile strategy for controllable synthesis of stable mesoporous black TiO₂ hollow spheres with efficient solar-driven photocatalytic hydrogen evolution. *J. Mater. Chem. A* **4**, 7495-7502 (2016).
- 54 Mao, C. Y., Zuo, F., Hou, Y., Bu, X. H. & Feng, P. Y. In situ preparation of a Ti³⁺ self-doped TiO₂ film with enhanced activity as photoanode by N₂H₄ reduction. *Angew. Chem. Int. Ed.* **53**, 10485-10489 (2014).
- 55 Van de Krol, R., Goossens, A. & Schoonman, J. Mott-Schottky analysis of nanometer-scale thin-film anatase TiO₂. *J. Electrochem. Soc.* **144**, 1723-1727 (1997).
- 56 Parker, R. A. Static dielectric constant of rutile (TiO₂), 1.6-1060°K. *Phys. Rev.* **124**, 1719-1722 (1961).
- 57 Low, J. X., Yu, J. G., Jaroniec, M., Wageh, S. & Al-Ghamdi, A. A. Heterojunction photocatalysts. *Adv. Mater.* **29**, 1601694 (2017).
- 58 Kresse, G. & Joubert, D. From ultrasoft pseudopotentials to the projector augmented-wave method. *Phys. Rev. B* **59**, 1758 (1999).

- 59 Kresse, G. & Furthmüller, J. Efficient iterative schemes for ab initio total-energy calculations using a plane-wave basis set. *Phys. Rev. B* **54**, 11169 (1996).
- 60 Perdew, J. P., Burke, K. & Ernzerhof, M. Generalized gradient approximation made simple. *Phys. Rev. Lett.* **77**, 3865-3868 (1996).
- 61 Monkhorst, H. J. & Pack, J. D. Special points for Brillouin-zone integrations. *Phys. Rev. B* **13**, 5188-5192 (1976).
- 62 Jiang, Z. *et al.* Filling metal-organic framework mesopores with TiO₂ for CO₂ photoreduction. *Nature* **586**, 549-554 (2020).
- 63 Butburee, T. *et al.* Improved CO₂ photocatalytic reduction using a novel 3-component heterojunction. *Nano Energy* **62**, 426-433 (2019).
- 64 Yang, J. *et al.* A comparative study on the photocatalytic behavior of graphene-TiO₂ nanostructures: Effect of TiO₂ dimensionality on interfacial charge transfer. *Chem. Eng. J.* **334**, 907-921 (2018).
- 65 Liu, Y. N. *et al.* Synergetic promotional effect of oxygen vacancy-rich ultrathin TiO₂ and photochemical induced highly dispersed Pt for photoreduction of CO₂ with H₂O. *Appl. Catal. B Environ.* **244**, 919-930 (2019).
- 66 Wang, W. N. *et al.* Size and structure matter: enhanced CO₂ photoreduction efficiency by size-resolved ultrafine Pt nanoparticles on TiO₂ single crystals. *J. Am. Chem. Soc.* **134**, 11276-11281 (2012).
- 67 Wang, Q. L. *et al.* Photoreduction of CO₂ using black TiO₂ films under solar light. *J. CO₂ Util.* **12**, 7-11 (2015).
- 68 Tahir, M., Tahir, B. & Amin, N. A. S. Gold-nanoparticle-modified TiO₂ nanowires for plasmon-enhanced photocatalytic CO₂ reduction with H₂ under visible light irradiation. *Appl. Surf. Sci.* **356**, 1289-1299 (2015).
- 69 Tahir, M., Tahir, B., Amin, N. A. S. & Zakaria, Z. Y. Photo-induced reduction of CO₂ to CO with hydrogen over plasmonic Ag-NPs/TiO₂ NWs core/shell hetero-junction under UV and visible light. *J. CO₂ Util.* **18**, 250-260 (2017).
- 70 Tahir, B., Tahir, M. & Amin, N. A. S. Photocatalytic CO₂ reduction to CO over Fe-loaded TiO₂/nanoclay photocatalyst. *Chem. Engin. Trans.* **56**, 1111-1116 (2017).

Declarations

Acknowledgements

This work was supported by National Key R&D Program of China (No. 2018YFE0208500) and NSF of China (Nos. 21972065, 21773114).

Author contributions

J.L. and D.W. conceived and designed the experiments. J.L. prepared photocatalysts and conducted most of all the experiments. L.W. carried out the photocatalytic test. W.S. and W.M. performed the theoretical calculation. J.L., D.W., and Y.Z. wrote and revised the manuscript. J.L., J.R., and S.Z. offered help to analyse the characterization experiment data. D.W. and Y.Z. gave suggestions on the experiment and writing. All authors discussed the results and commented on the manuscript.

Competing interests

The authors declare no competing interests.

Table

Table 1. Comparison of the CO yield rate of this work with that of other reported TiO₂-based photocatalysts.

Photocatalysts	Yield rate ($\mu\text{mol g-cat}^{-1} \text{ h}^{-1}$)	Reaction environment	Light sources (Intensity)	Reference
Au / TiO ₂ / Pt Film (LRS)	CO : 1729	CO ₂ and H ₂ O vapor	300 W Xe lamp	This work
Au / TiO ₂ / Pt Film (HRS)	CO : 1007	CO ₂ and H ₂ O vapor	300 W Xe lamp	This work
42%-TiO ₂ -in-MIL-101-Cr-NO ₂	CO : 12000	CO ₂ and H ₂ O vapor	300 W Xe lamp	62
3J-TiO ₂ / AuCu / ZIF-8 Film	CO : 83	CO ₂ and H ₂ O vapor	300 W Xe lamp	63
GR-TiO ₂	CO : 75.8	CO ₂ and H ₂ O vapor	300 W Xe lamp	64
Pt nanoparticles loaded ultrathin TiO ₂ nanosheets	CO : 54.2	CO ₂ and H ₂ O vapor	300 W Xe lamp	65
1wt.% Pt / TiO ₂ Film	CO : 200	CO ₂ and H ₂ O vapor	400 W Xe lamp	66
black TiO ₂ Film with grid-like structure	CO : 115	CO ₂ and H ₂ O vapor	Two 300 W Xe lamp	67
0.5wt.-%-Au / TiO ₂ NWs	CO : 1237	CO ₂ and H ₂	35 W Xe lamp	68
Ag / TiO ₂ NWs	CO : 983	CO ₂ and H ₂	200 W Hg lamp	69
3% Fe-10% MMT / TiO ₂	CO : 289.3	CO ₂ and H ₂	200 W Hg lamp	70

Figures

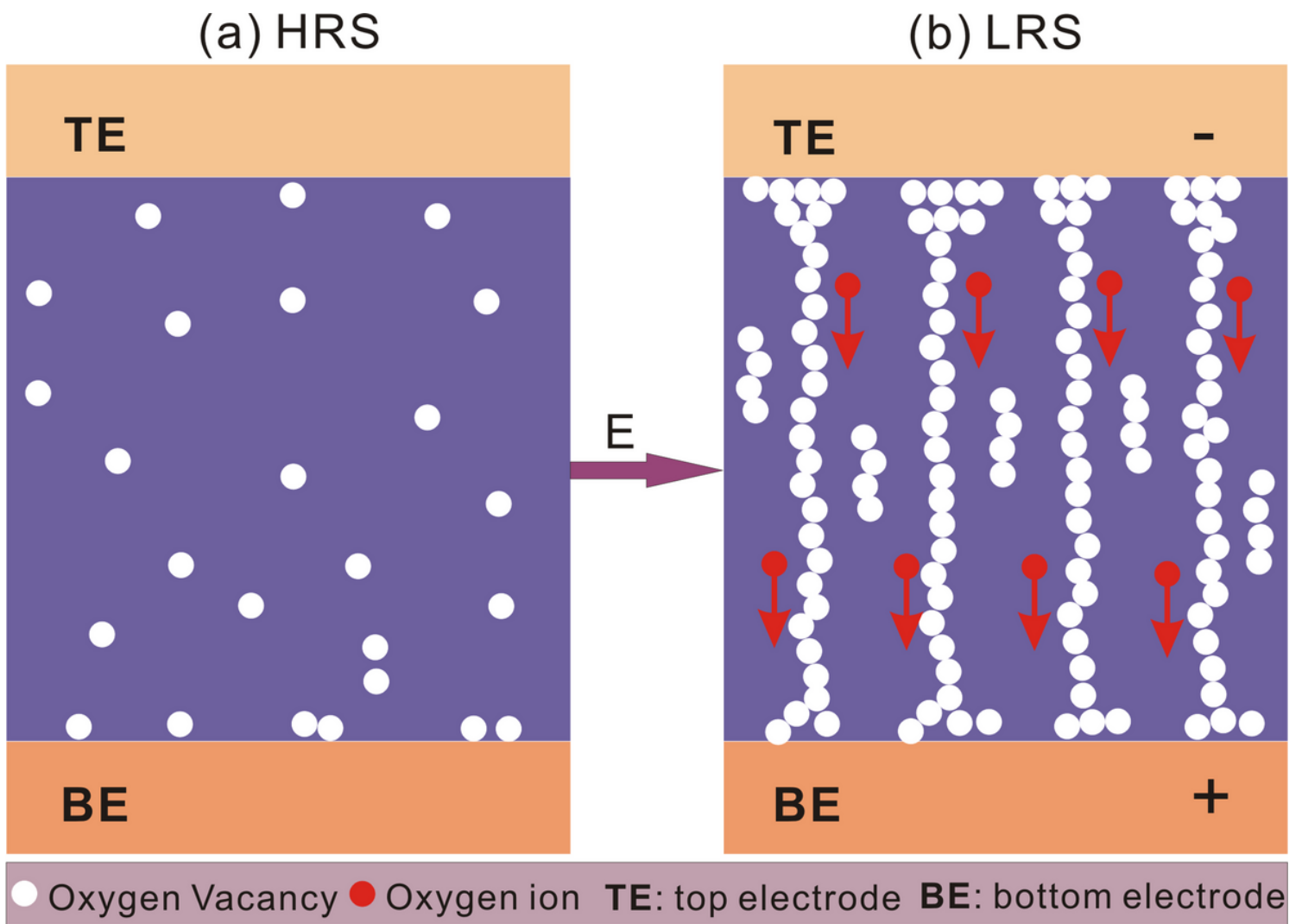


Figure 1

Schematic diagram of resistance switching (RS) mechanism. a high resistance state (HRS) and b low resistance state (LRS).

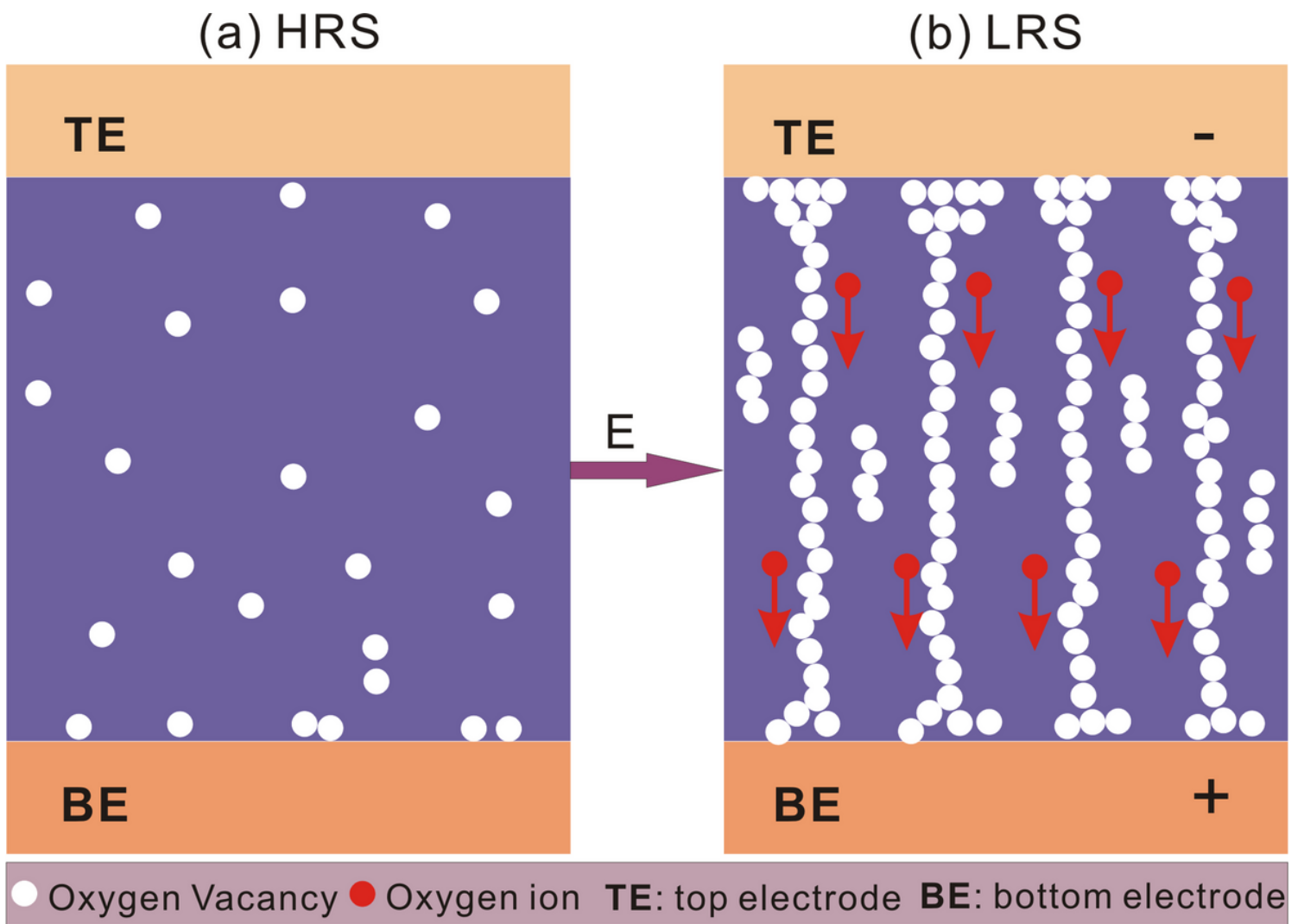


Figure 1

Schematic diagram of resistance switching (RS) mechanism. a high resistance state (HRS) and b low resistance state (LRS).

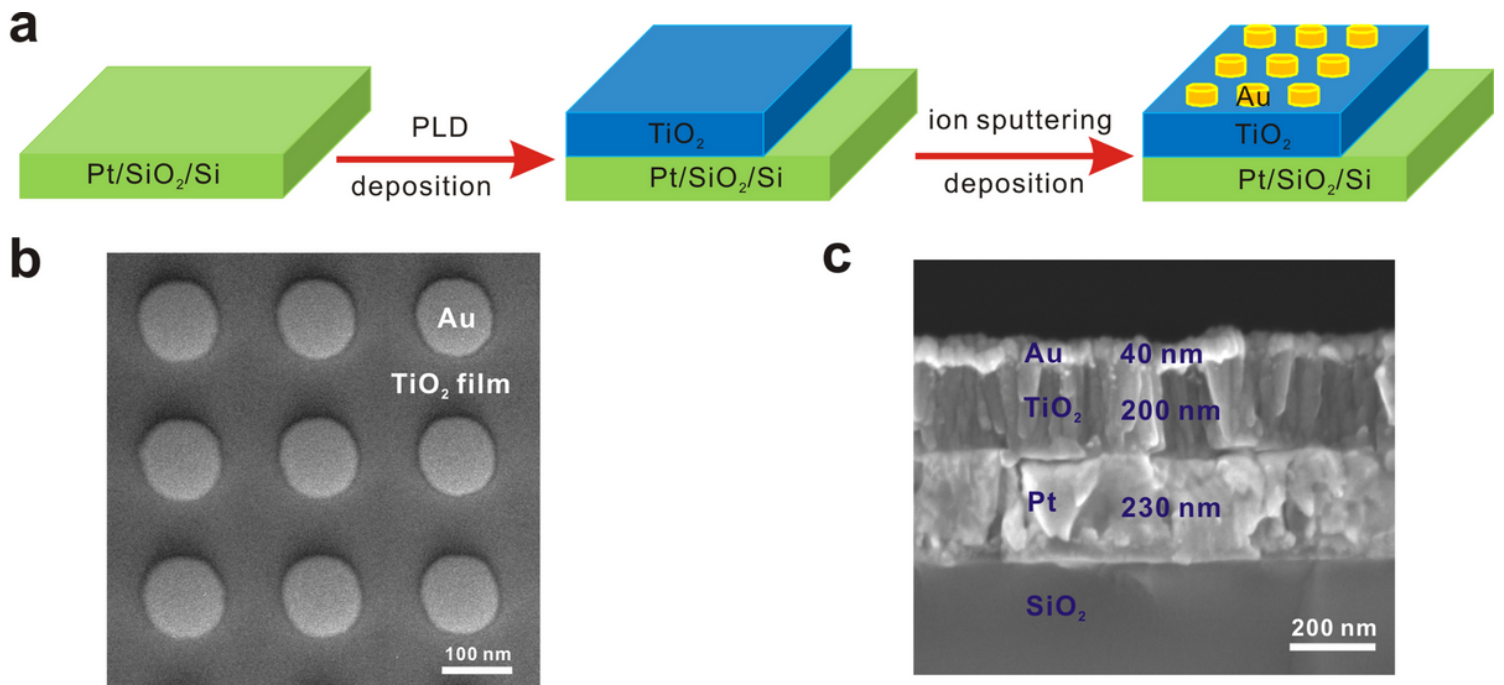


Figure 2

The schematic diagrams and structural characterizations. a Schematic image of formation process, b SEM images of the surface and c Cross section of Au/TiO₂/Pt device.

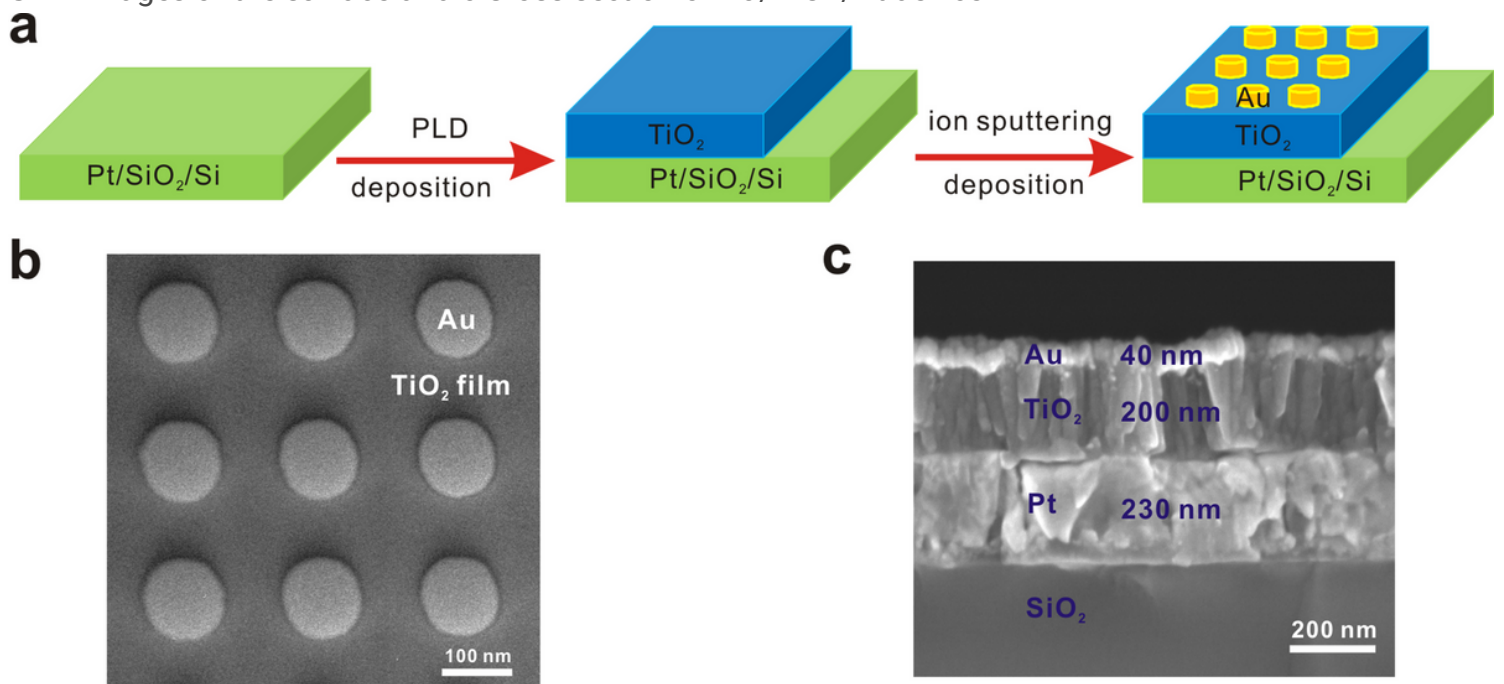


Figure 2

The schematic diagrams and structural characterizations. a Schematic image of formation process, b SEM images of the surface and c Cross section of Au/TiO₂/Pt device.

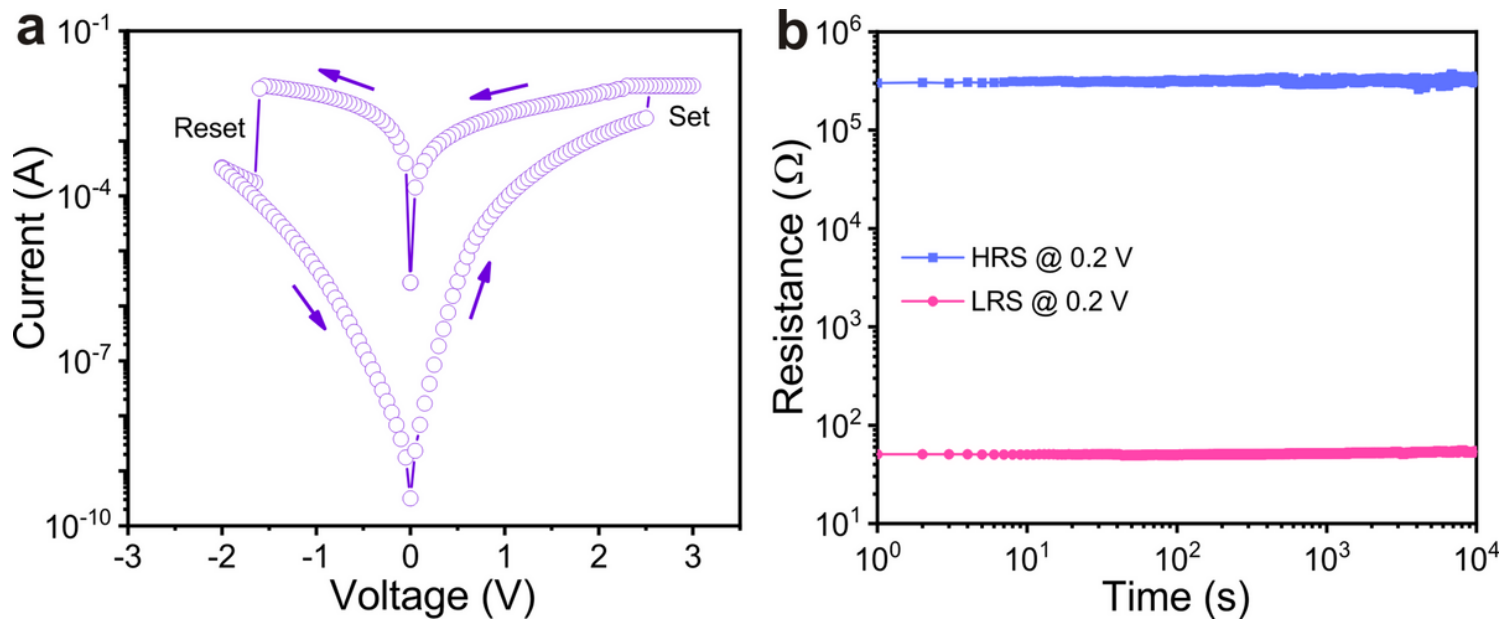


Figure 3

RS characteristic. a I-V curve and b Endurance test of the RS device.

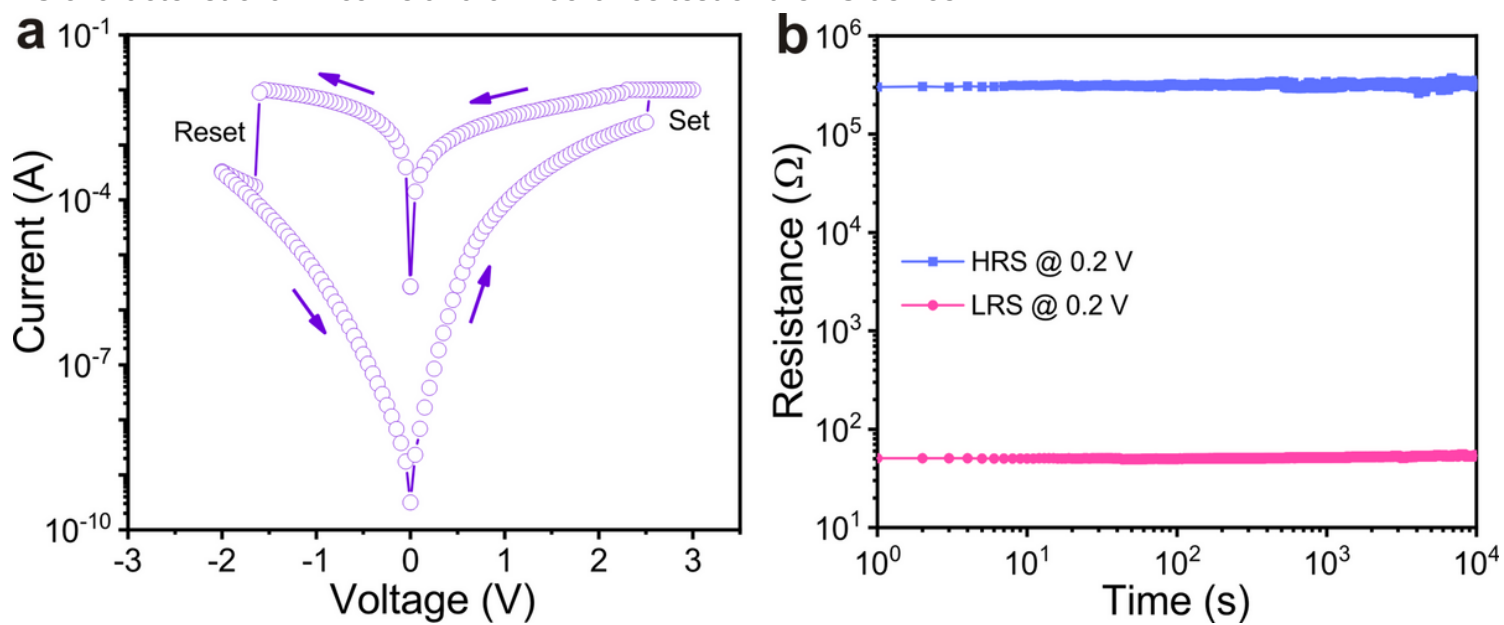


Figure 3

RS characteristic. a I-V curve and b Endurance test of the RS device.

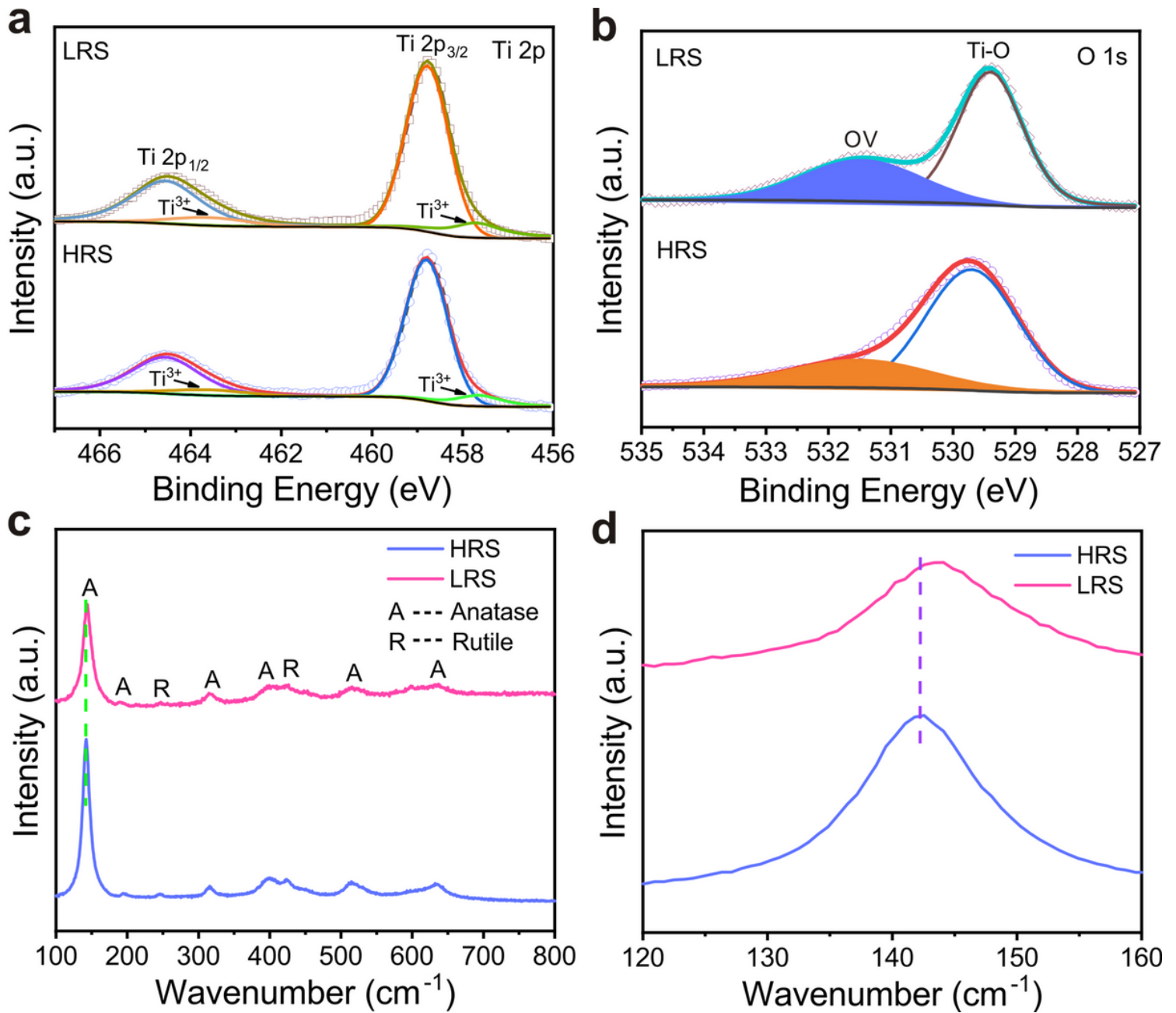


Figure 4

Characterizations of structure and oxygen vacancy. a XPS spectra in Ti 2p level and b O 1s level of LRS and HRS samples. c Raman spectra of LRS and HRS samples with the excitation line at 532 nm. d The corresponding enlarged Raman spectra from 120 to 160 cm⁻¹.

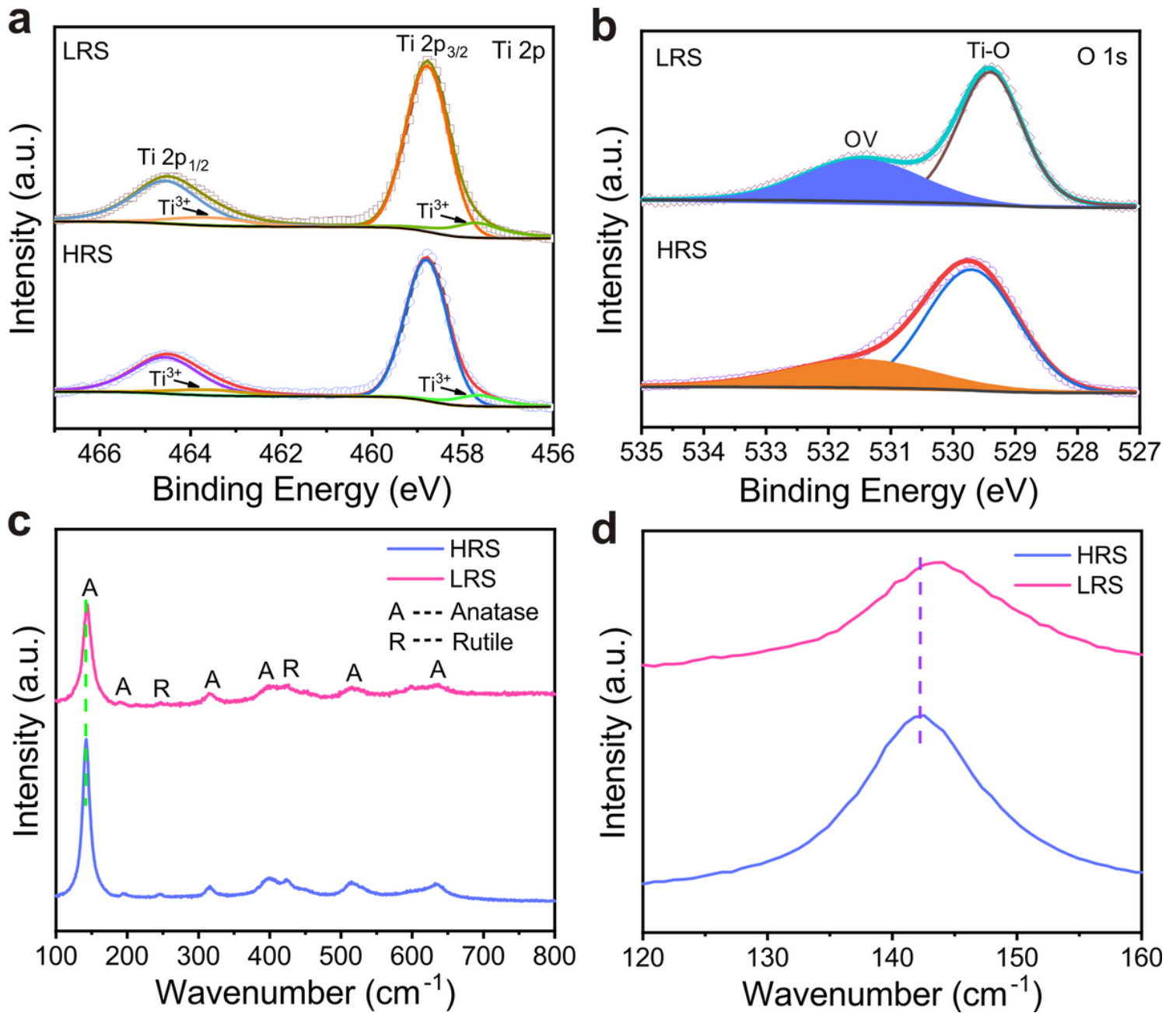


Figure 4

Characterizations of structure and oxygen vacancy. a XPS spectra in Ti 2p level and b O 1s level of LRS and HRS samples. c Raman spectra of LRS and HRS samples with the excitation line at 532 nm. d The corresponding enlarged Raman spectra from 120 to 160 cm⁻¹.

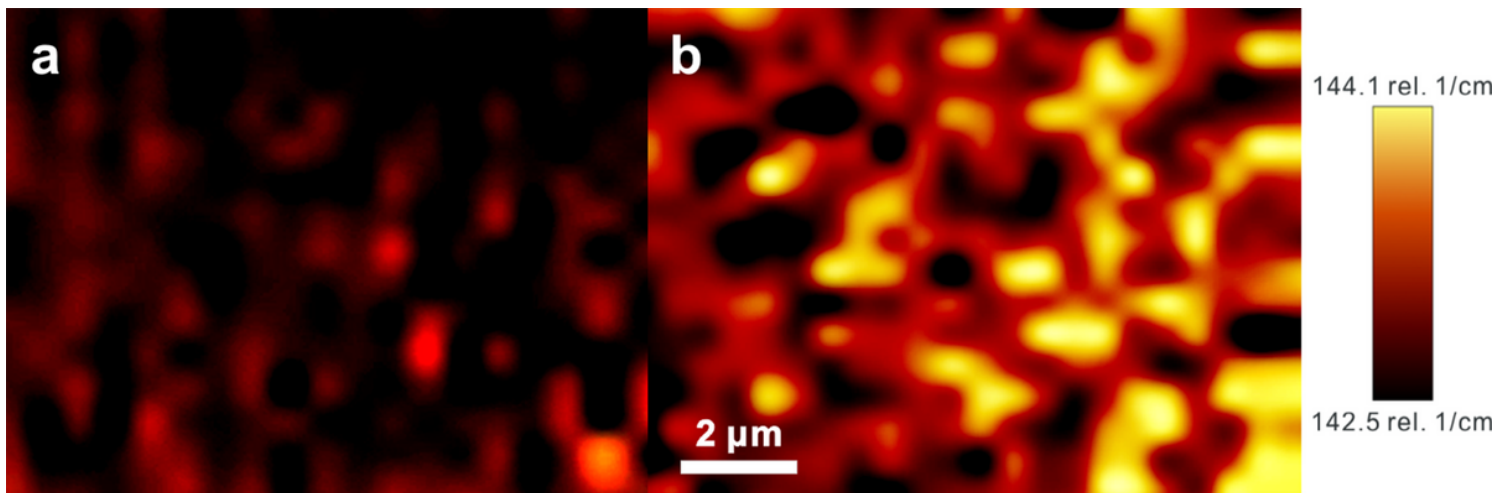


Figure 5

The distribution of oxygen vacancies. Two-dimensional Raman spectrum at 143 cm⁻¹ of a HRS sample and b LRS sample after etching. The brightness represents the wavenumber.

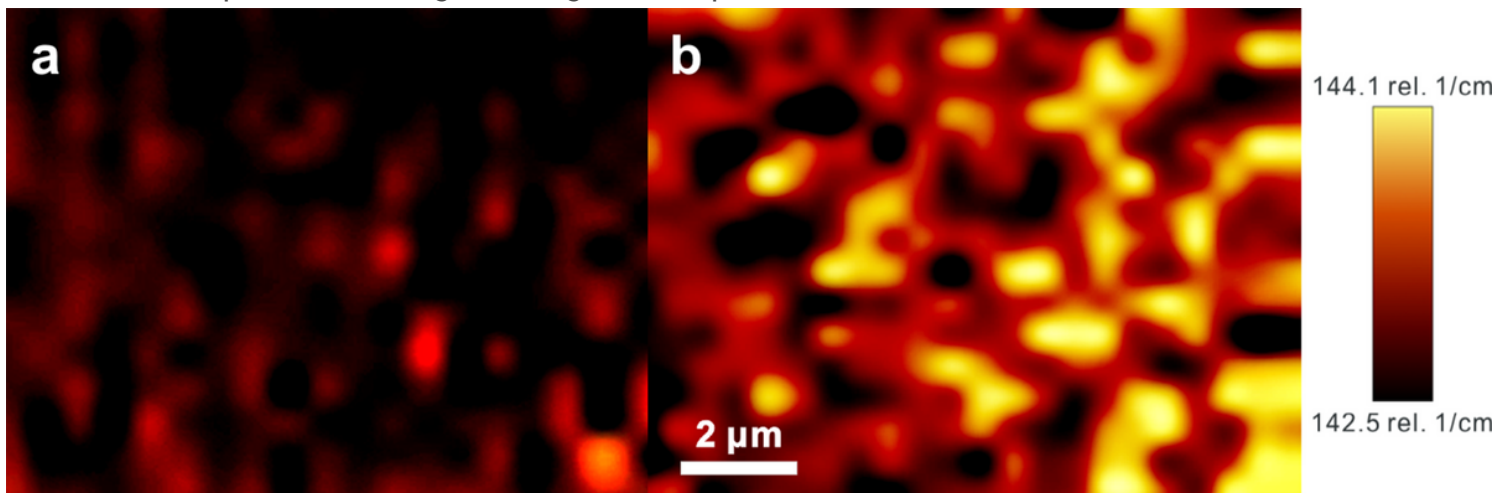


Figure 5

The distribution of oxygen vacancies. Two-dimensional Raman spectrum at 143 cm⁻¹ of a HRS sample and b LRS sample after etching. The brightness represents the wavenumber.

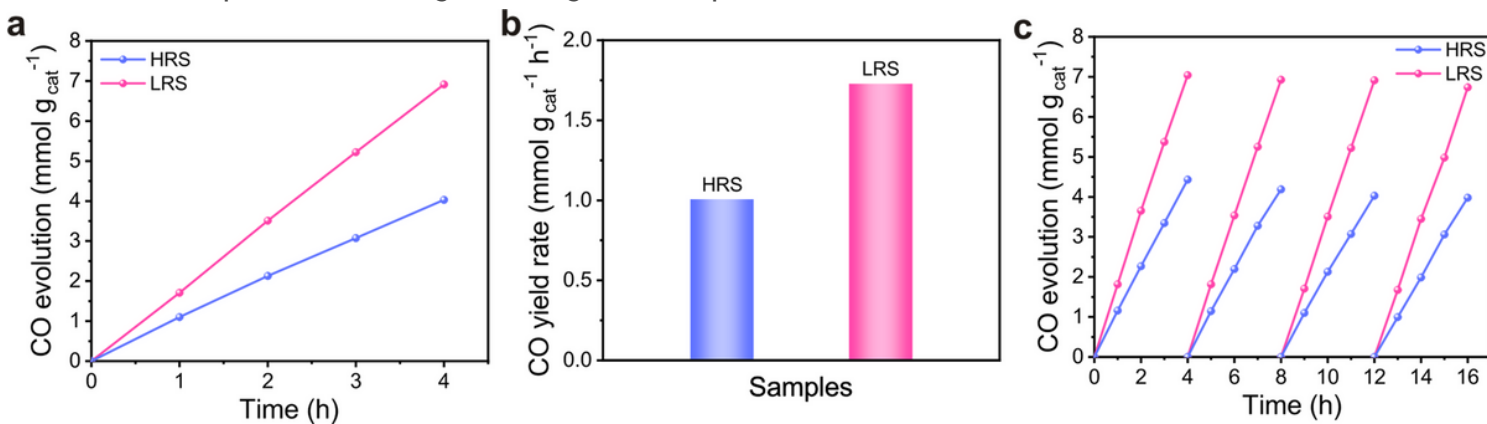


Figure 6

Photocatalytic performance of CO₂ reduction. a Time course evolution of CO for 4h with 300 W Xe lamp and b CO yield rate of LRS and HRS samples. c Cycle experiment of photocatalytic CO₂ reduction. g_{cat}: The mass of TiO₂ film catalyst.

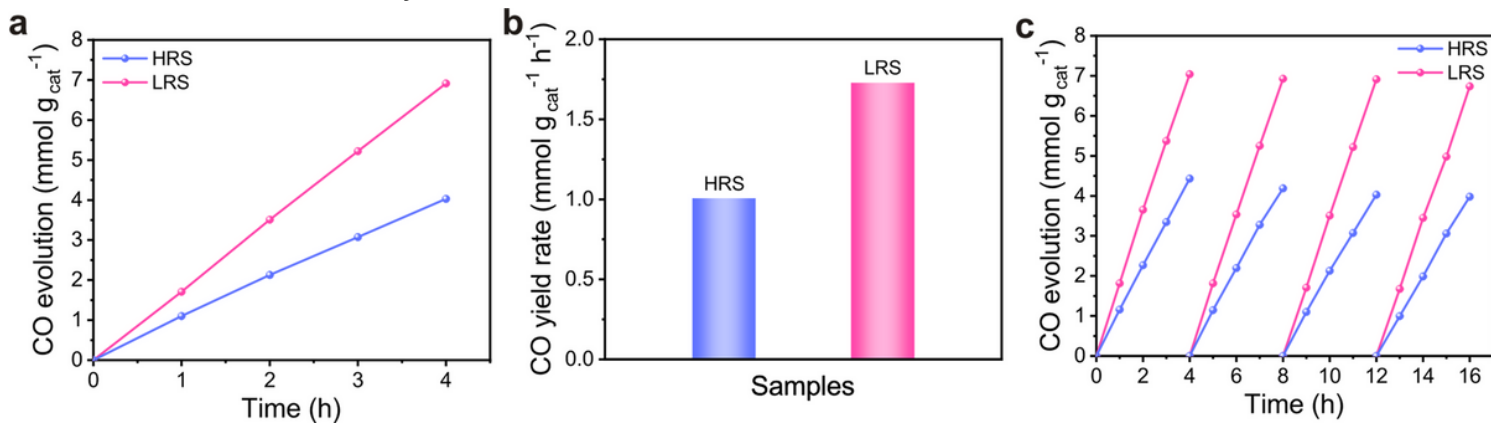


Figure 6

Photocatalytic performance of CO₂ reduction. a Time course evolution of CO for 4h with 300 W Xe lamp and b CO yield rate of LRS and HRS samples. c Cycle experiment of photocatalytic CO₂ reduction. g_{cat}: The mass of TiO₂ film catalyst.

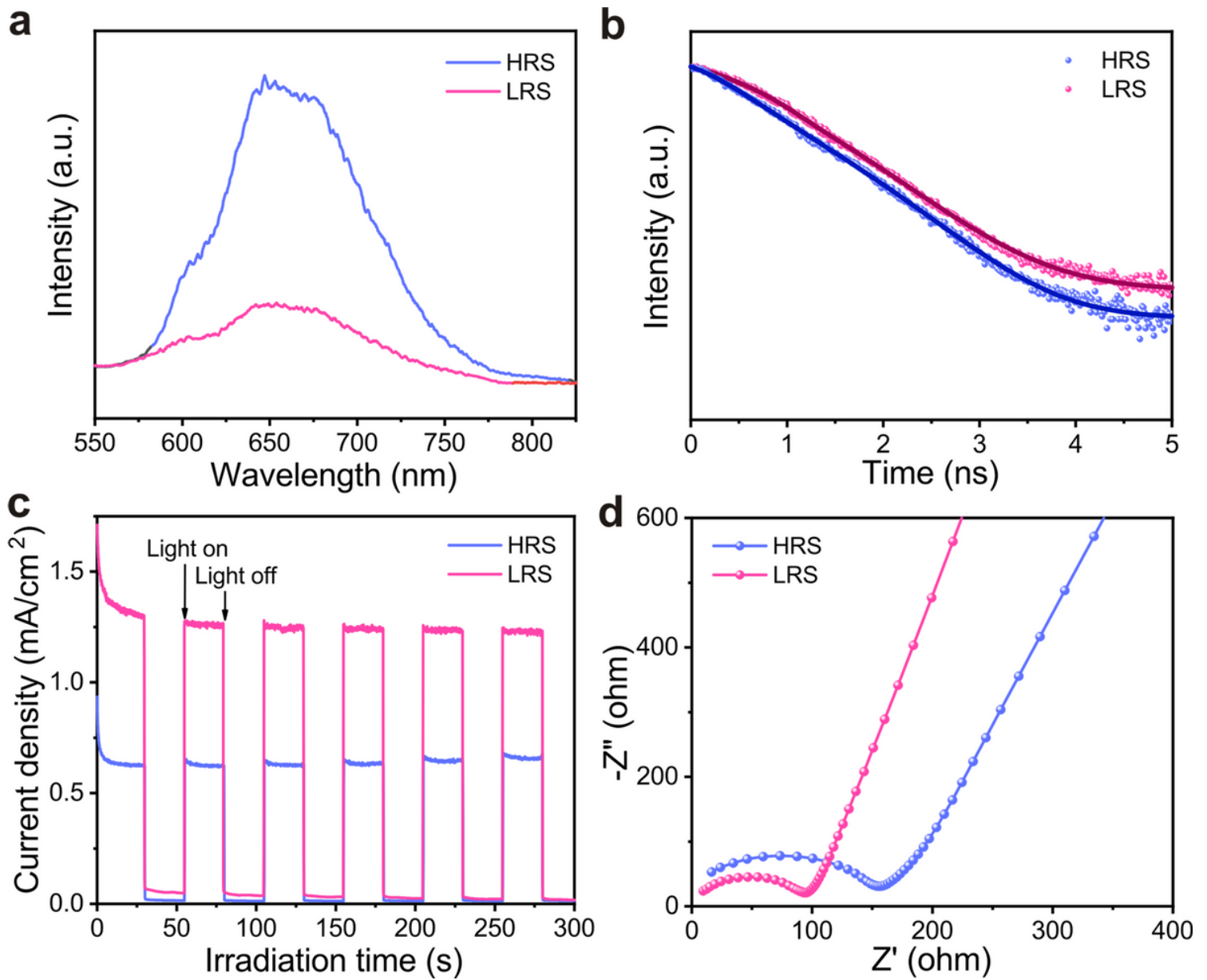


Figure 7

Separation efficiency of carriers. a Photoluminescence emission spectra with excitation at 532 nm. b Time-resolved photoluminescence spectroscopy of HRS and LRS samples. c The transient chronoamperometry with the measurement conditions: 0.1 M sodium sulfate solution, the bias potential is 0.6 V, the switching time interval is 25 s. d The Nyquist plots of the electrochemical impedance spectroscopy.

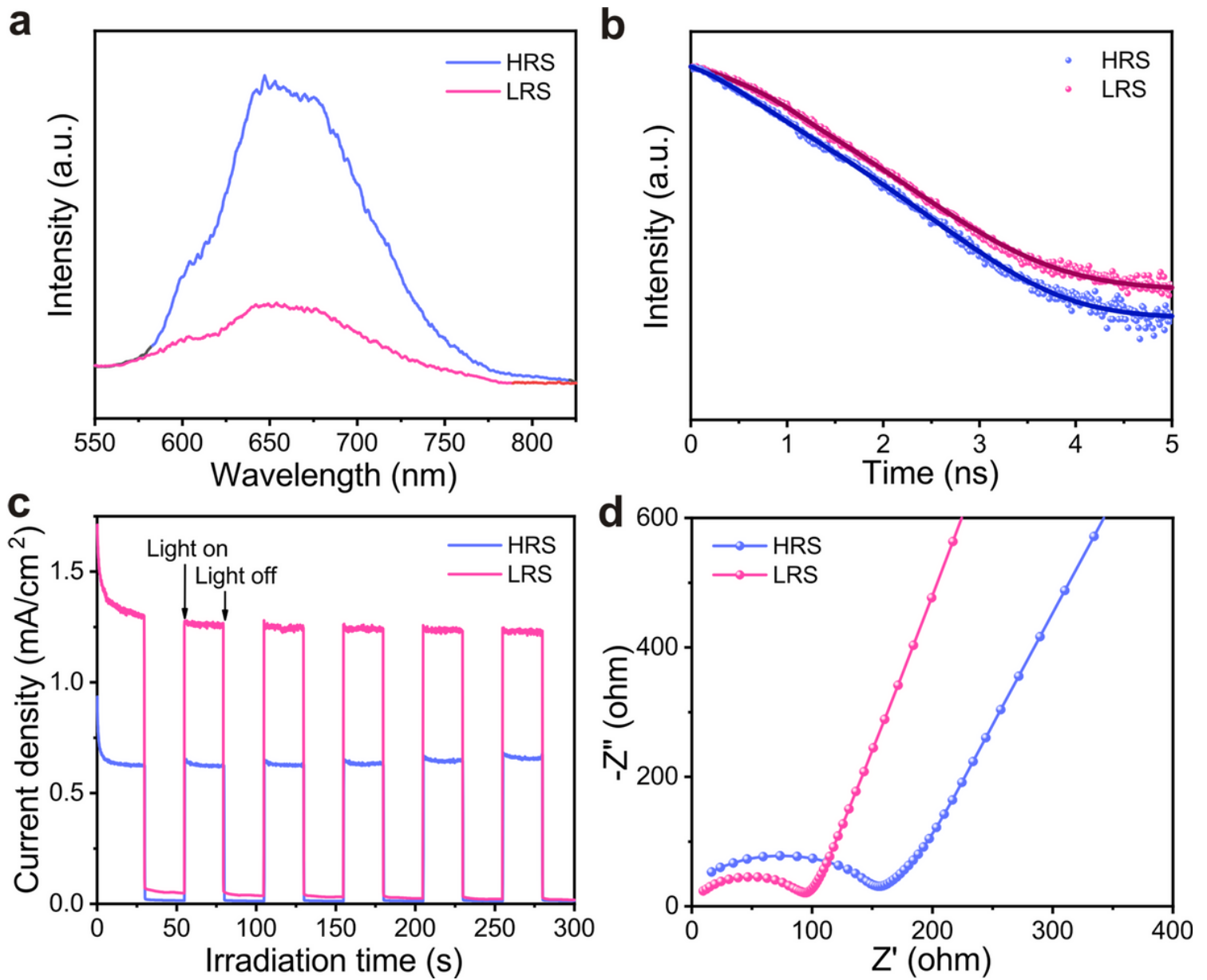


Figure 7

Separation efficiency of carriers. a Photoluminescence emission spectra with excitation at 532 nm. b Time-resolved photoluminescence spectroscopy of HRS and LRS samples. c The transient chronoamperometry with the measurement conditions: 0.1 M sodium sulfate solution, the bias potential is 0.6 V, the switching time interval is 25 s. d The Nyquist plots of the electrochemical impedance spectroscopy.

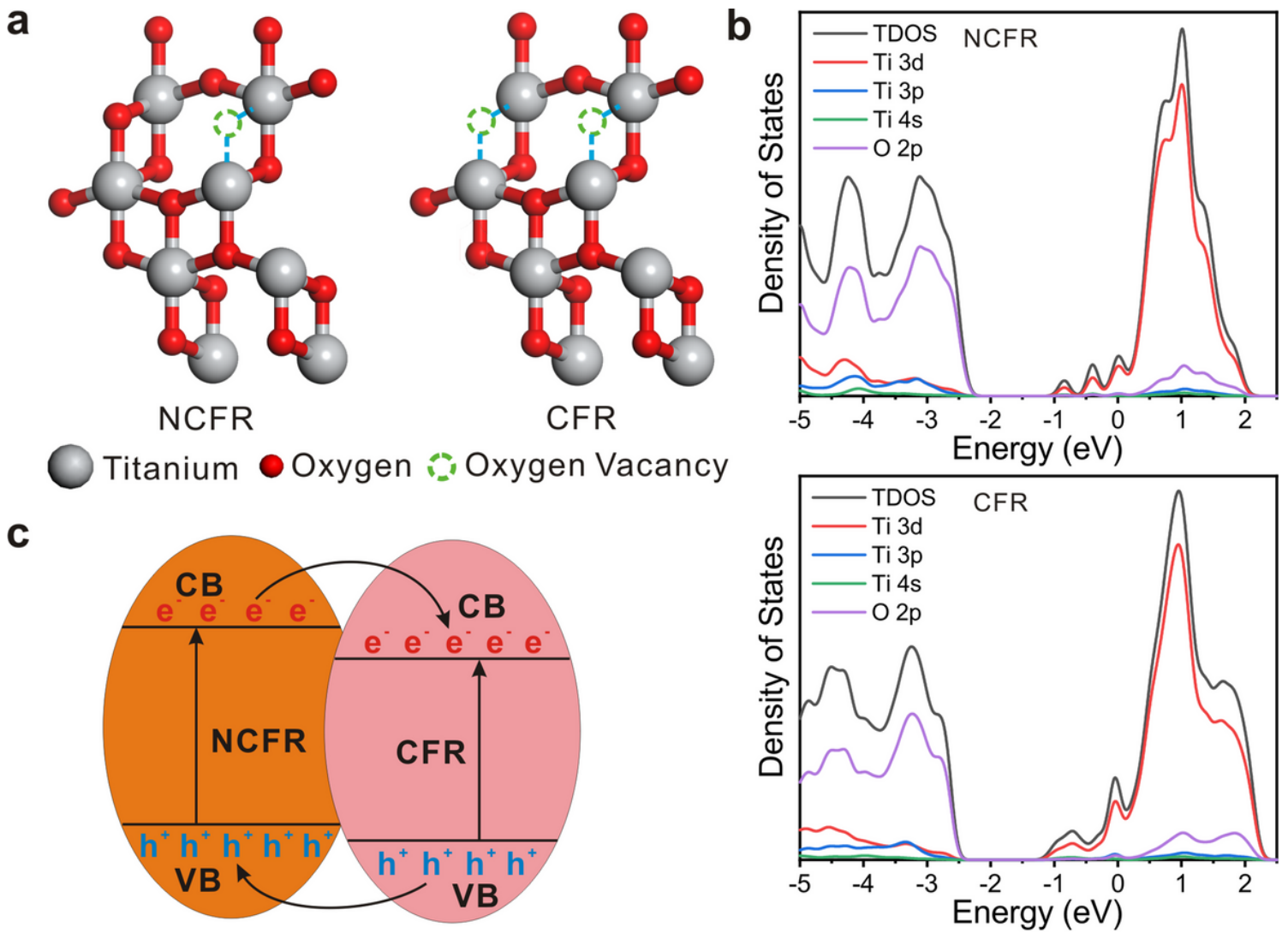


Figure 8

DFT calculation for electronic structure and the formation of homojunction. The anatase structure is used for DFT calculation due to the main component of the prepared TiO₂ film is anatase. a The structure models of 2'1'1 supercell for anatase TiO₂ with different concentrations of OVs: One OV per 16 O atoms (NCFR) and Two OVs per 16 O atoms (CFR), respectively. Titanium atom, oxygen atom and oxygen vacancy are represented by grey sphere, red sphere and green dotted circle, respectively. b Calculated density of states for anatase with different OV concentrations. c Schematic diagram of homojunction between CFR and NCFR in LRS sample.

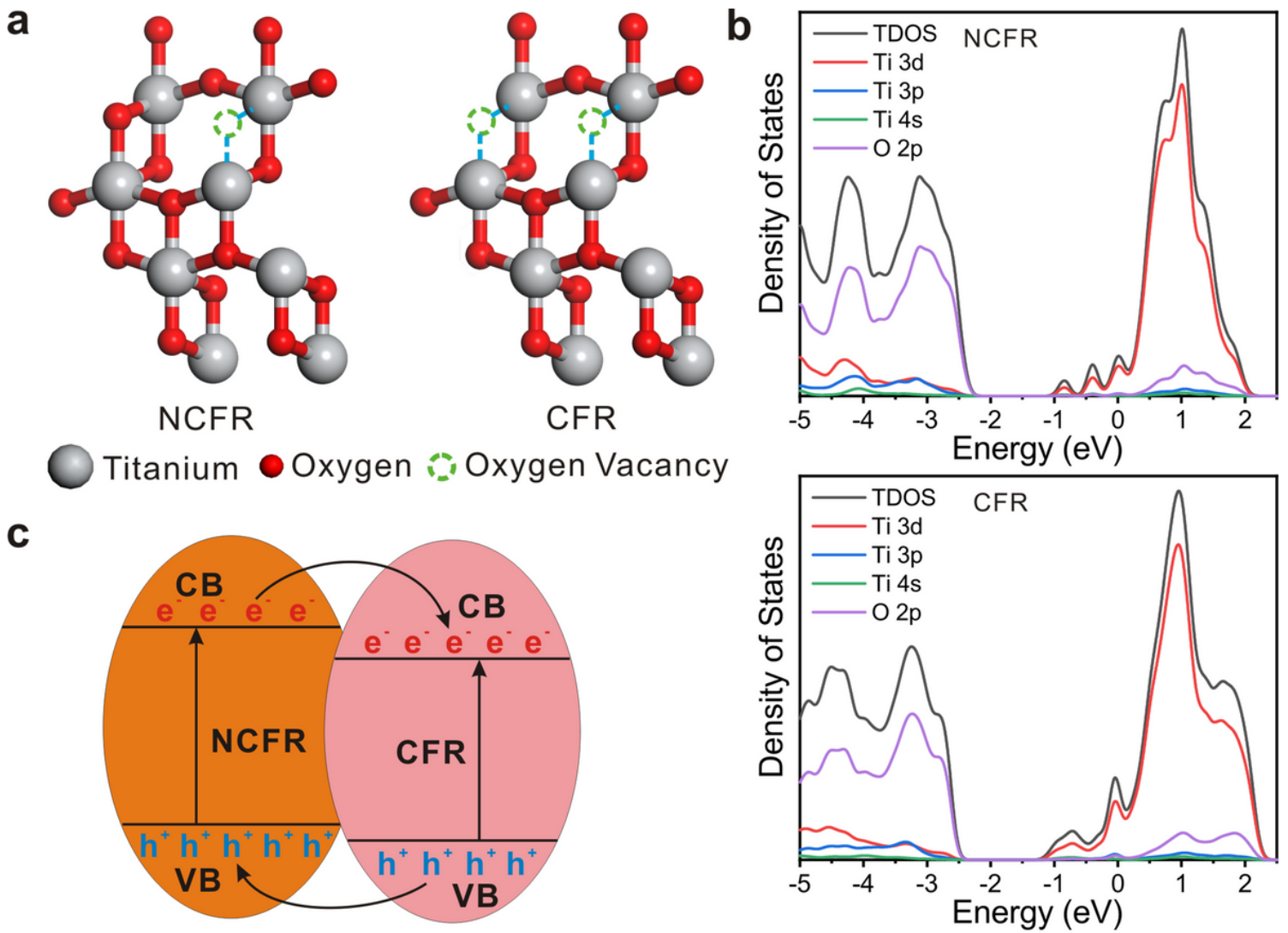


Figure 8

DFT calculation for electronic structure and the formation of homojunction. The anatase structure is used for DFT calculation due to the main component of the prepared TiO₂ film is anatase. a The structure models of 2'1'1 supercell for anatase TiO₂ with different concentrations of OVs: One OV per 16 O atoms (NCFR) and Two OVs per 16 O atoms (CFR), respectively. Titanium atom, oxygen atom and oxygen vacancy are represented by grey sphere, red sphere and green dotted circle, respectively. b Calculated density of states for anatase with different OV concentrations. c Schematic diagram of homojunction between CFR and NCFR in LRS sample.

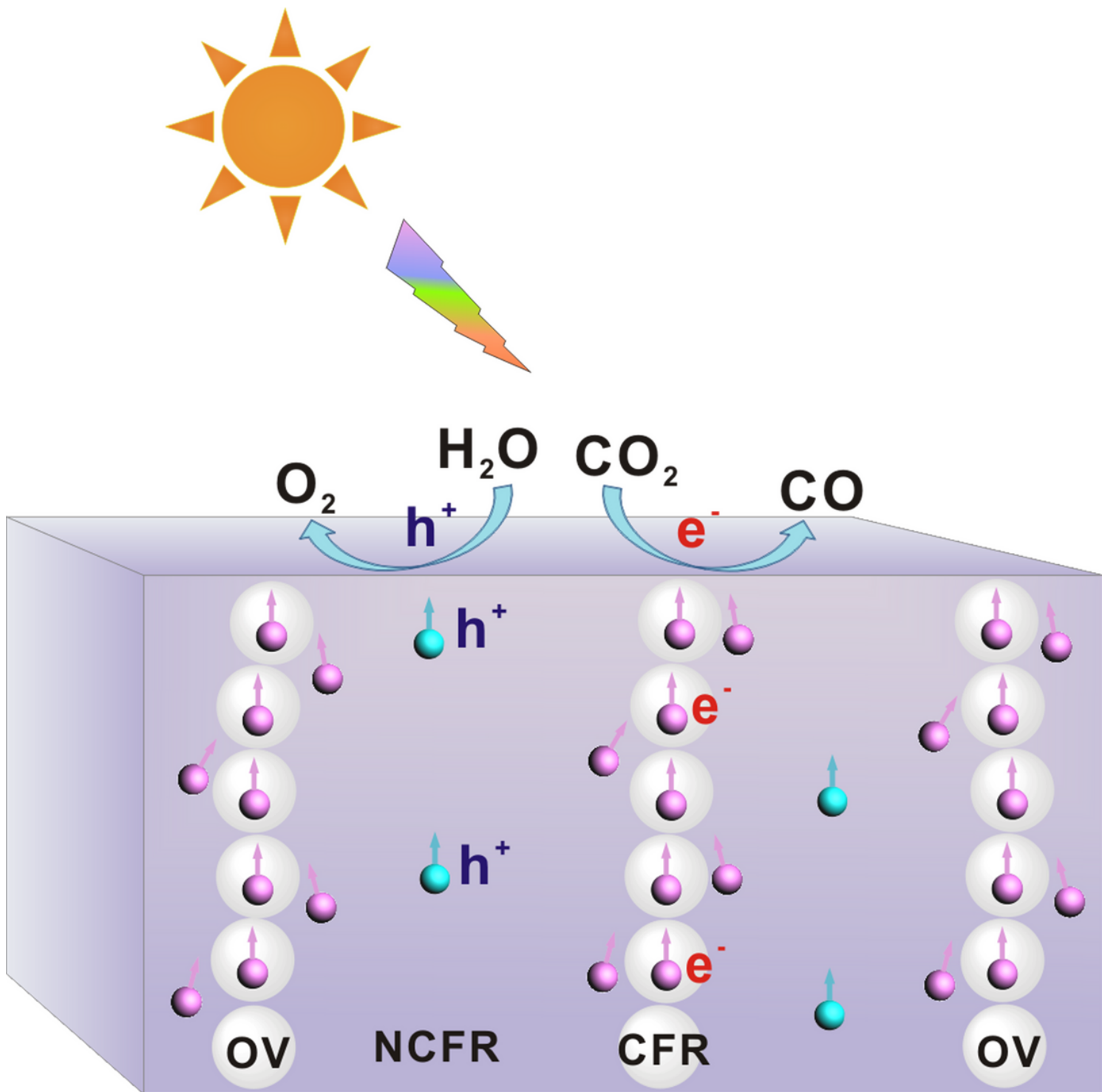


Figure 9

The photocatalytic mechanism of LRS system for CO₂ reduction.

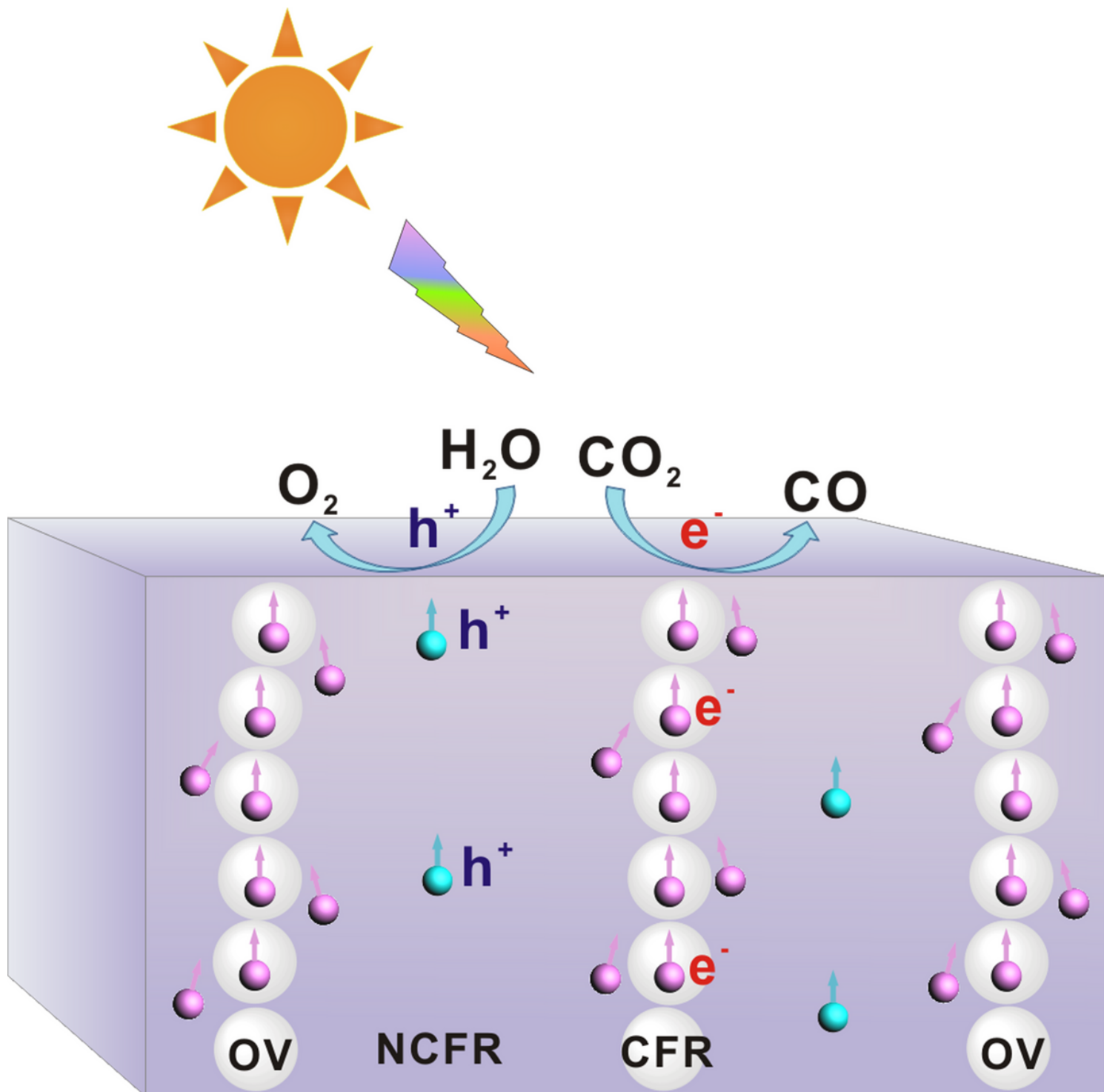


Figure 9

The photocatalytic mechanism of LRS system for CO₂ reduction.

Supplementary Files

This is a list of supplementary files associated with this preprint. Click to download.

- [SupplementaryInformation.docx](#)

- [SupplementaryInformation.docx](#)